Journal of Molecular Catalysis A: Chemical 289 (2008) 69–75

Contents lists available at ScienceDirect

Journal of Molecular Catalysis A: Chemical

journal homepage: www.elsevier.com/locate/molcata

Investigation of Fe–P–B ultrafine amorphous nanomaterials: Influence of synthesis parameters on physicochemical and catalytic properties

Baskaran Rajesh, Natarajan Sasirekha, Shao-Pai Lee, Hsin-Yi Kuo, Yu-Wen Chen*

Department of Chemical Engineering, National Central University, Chung-Li 320, Taiwan, ROC

ARTICLE INFO

Article history:
Received 27 July 2007
Received in revised form 31 March 2008
Accepted 15 April 2008
Available online 23 April 2008

Keywords:
Nanoalloys
Fe–P–B
TEM
Solvent effect

ABSTRACT

A series of Fe–P–B ultrafine amorphous alloy particles were synthesized by chemical reduction method to study the influence of iron precursors such as $FeCl_2{\cdot}4H_2O$, $FeCl_3{\cdot}6H_2O$, and $Fe(OAc)_2$ and reaction medium (H_2O, 50% ethanolic solution, and 50% isopropyl alcoholic solution). The physicochemical properties of the as-synthesized materials were characterized by X-ray diffraction, inductively coupled plasma-atomic emission spectroscopy, N_2 sorption, transmission electron microscopy, X-ray photoelectron spectroscopy, and electron diffraction. The existence of amorphous nature of Fe–P–B materials was found to be retained even when the temperature was up to 300 °C. Use of different iron precursors and solvents in the preparation significantly influenced the structure, morphology, and composition of Fe–P–B nanoalloys. Dehydrogenation of ethanol has been carried out in order to evaluate the catalytic properties of the Fe–P–B nanoalloys and the results have been related to the surface properties of Fe–P–B nanoalloys. Fe–P–B prepared with $FeCl_2$ in 50% ethanolic solution, showed the highest activity among all the Fe–P–B catalysts.

1. Introduction

Amorphous alloys and nanomaterials have attracted extensive attention due to their special properties that lead to important attainable and potential applications in various fields such as, powder metallurgy, magnetic recording, ferrofluids and catalysis, etc. The presence of high concentrations of highly coordinatively unsaturated sites on these amorphous alloys facilitates adsorption and surface reactions compared to their corresponding crystalline catalysts. The nonporous nature of these materials eliminates the effects of intraparticle limitations on the surface reactions. Since the introduction of rapid quenching techniques [1] for producing metal–metalloid amorphous alloys, the metastable materials with short-range ordering structure have attracted a considerable attention due to their superior electronic, magnetic, mechanical, and chemical properties [2,3]. The classical works by Yamashita et al. and Masumoto et al. [4–14] on the hydrogenation of carbon monoxide motivated rapid growth in research into amorphous alloy catalysis.

Since Schlesinger et al. [15] successfully prepared nickel boride catalysts in aqueous and ethanolic solutions, by reacting an inorganic nickel salt and sodium borohydride, metal borides have attracted extensive interest. Some examples include M–B (M = Fe, Co, or Ni) [16–19]; Ni–P [20–25]; Co–P [25]; Fe–P–B [26–28]; Ni–P–B [29]; Fe–P [30].

Transition metal boron amorphous particles have been prepared by reducing metal ions to their metallic state by use of an alkali metal borohydride, usually in an aqueous solution. The composition of the particles depends on the preparation parameters such as the order of the mixing reactants, adding rates, concentration, pH, and temperature. Among these parameters, the temperature seems to play a vital role in altering the B content, which could be correlated with the activation energy of the reaction [31]. We have recently reported the effect of synthesis parameters on the characteristics of Fe–B nanoalloys for dehydrogenation of ethanol [32]. Electrochemical preparation of Fe–P alloys have been reported under relatively simple experimental conditions. The electrochemical deposition of thin films of Fe–P alloys was carried out under various experimental conditions and their composition, structure, and electrochemical properties were investigated and reported. Studies on Fe and P K edges in a series of $Fe_{100-x}P_x$ amorphous alloys and changes in the short-range order with sample composition were correlated with the magnetic properties by Fdez-Gubieda et al. [33]. The synthesis of Fe–P nanoparticles from $Fe(acac)_3$ and $P(SiMe_3)_3$ as a phase-pure, discrete particles and the effect of the nanosized dimensions on the resultant magnetic properties were investigated by Perera et al. [34]. A systematic analysis of the effects of B and P concentrations on the pore distribution, on the coordination number distribution, and the interatomic distance in amorphous Fe–B and Fe–P alloys was investigated by Hoang [35].

* Corresponding author. Tel.: +886 3 4227151x34203; fax: +886 3 4252296.
E-mail address: ywchen@cc.ncu.edu.tw (Y.-W. Chen).

1381-1169/$ – see front matter © 2008 Elsevier B.V. All rights reserved.
doi:10.1016/j.molcata.2008.04.013

Table 1
Composition of Fe–P–B catalysts under various preparation conditions

Sample notation	Preparation conditions		Bulk composition[a] (atomic ratio)	Surface composition[b] (atomic ratio)
	Iron precursor	Solvent		
A	$FeCl_2{\cdot}4H_2O$	H_2O	$Fe_{75.6}P_{10.2}B_{14.2}$	$Fe_{81.7}P_{2.0}B_{15.3}$
B	$FeCl_3{\cdot}6H_2O$	H_2O	$Fe_{85.1}P_{2.1}B_{12.8}$	$Fe_{86.3}P_{1.2}B_{12.5}$
C	$FeCl_2{\cdot}4H_2O$	EtOH/H_2O (1:1)	$Fe_{82.4}P_{1.1}B_{16.5}$	$Fe_{84.5}P_{2.5}B_{13.0}$
D	$Fe(OAc)_2$	EtOH/H_2O (1:1)	$Fe_{87.3}P_{3.3}B_{9.4}$	$Fe_{83.1}P_{3.9}B_{13.0}$
E	$Fe(OAc)_2$	IPA/H_2O (1:1)	$Fe_{78.6}P_{8.8}B_{12.6}$	$Fe_{77.6}P_{7.1}B_{15.3}$

Fe/P/B ratio in the starting material is 1:3:3.
[a] Determined by ICP-AES.
[b] Determined by XPS.

Shen et al. [26] investigated the fundamental properties of $Fe_{82}P_{11}B_7$ produced by chemical reduction and its structure relaxation and crystallization after being annealed at various temperatures. Lin et al. [36] studied the effect of Sn, Al, and C additions into the $Fe_{80}P_{12}Si_4B_4$ alloy on the glass-forming ability, thermal properties, and soft magnetic properties. To our knowledge, very few reports were published on the preparation, properties, and applications of Fe–P–B nanoalloys. Our objective in the present study is to examine the effect of preparation parameters on the substitution of B for P and its influence on the catalytic activity of Fe–P–B nanoalloys for the dehydrogenation of ethanol.

2. Experimental

2.1. Catalyst preparation

Fe–P–B ultrafine amorphous alloy particles were systematically synthesized by chemical reduction method. Various iron salts such as $FeCl_2$, $FeCl_3$, and $Fe(OAc)_2$ were used as iron precursors. The solution of iron precursor (1000 ml, 0.1 M) and sodium hypophosphite (1 M) were mixed and the solution of sodium borohydride (1 M) was then added in drops into the mixture. The black precipitate, formed immediately was washed thoroughly with deionized water and with a 99% ethanol solution. It was then stored in a 99% ethanol solution.

2.2. Catalyst characterization

XRD analysis was performed using a Siemens D500 powder diffractometer. The XRD patterns were collected using Cu $K\alpha_1$ radiation (1.5405 Å) at a voltage and current of 40 kV and 30 mA, respectively. The sample was scanned over the range $2\theta = 20–60^\circ$ at a rate of 0.05 °/min to identify the amorphous nature. Samples for XRD were prepared as thin layers on a sample holder. Elemental analysis using inductively coupled plasma-atomic emission spectroscopy (ICP-AES) (Jobin-Yvon Company, France, JY-24) was carried out on the Fe–P–B samples to study the effect of preparation method on the compositions of the samples. In general, the weighed samples were dissolved in nitric acid and diluted with deionized water to concentrations within the calibration range of each element. The standard solutions purchased from Merck were diluted and used to establish the calibration curves. Wavelengths used for elemental analysis were 259.94 and 249.77 nm for Fe and P, respectively. N_2 sorption isotherms were measured at −197 °C using a Micromeritics ASAP 2010 instrument. Prior to the experiments, the samples were dehydrated at 100 °C until the vacuum pressure was below 0.1 Pa. The measurement of the surface areas of the samples was achieved by Brunauerr–Emmett–Teller (BET) method for relative pressures in the range $P/P_0 = 0.05–0.2$. The morphology and particle size of the samples were determined by transmission electron microscopy (TEM) on a Jeol JEM-2000 FX II instrument operated at 160 kV. Initially, a small amount of sample was placed into the sample tube filled with a 99% ethanol solution. After agitating under ultrasonic environment for 10 min, one drop of the dispersed slurry was dipped onto a carbon-coated copper mesh (300#) (Ted Pella Inc., CA, USA), and dried in an oven at 100 °C for 1 h. XPS spectra were recorded on a Thermo VG Scientific Sigma Probe spectrometer. The XPS patterns were collected using Al Kα radiation at a voltage and current of 20 kV and 30 mA, respectively. The base pressure in the analyzing chamber was maintained in the order of 10^{-9} Torr. The spectrometer was operated at 23.5 eV pass energy. The binding energy of XPS was corrected by contaminant carbon (C_{1s} = 285.0 eV) in order to facilitate the comparisons of the values among the catalysts and the standard compounds.

2.3. Catalytic activity

The dehydrogenation reaction was carried out in a continuous, U-shaped, quartz microreactor. About 40 mg of fresh catalyst was placed on a layer of quartz wool. The catalyst was first reduced with 5% H_2 in Ar at 250 °C for 30 min. A saturator containing 99.8% ethanol was kept at a constant temperature of 22 °C. Nitrogen was used as a carrier gas at a constant flow rate of 40 ml/min. The experiments were carried out at a constant temperature of 250 °C under atmospheric pressure. To prevent possible condensation of reactant and products, all connection gas lines and valves were analyzed by a China Chromatography 8900F gas chromatograph with a thermal conductivity detector. The column was 5 m long and packed with Hyesep D, which was maintained at 150 °C. Product gas concentrations were determined with a SCSC2.01 integrator by comparing the peak areas with those of a standard mixture.

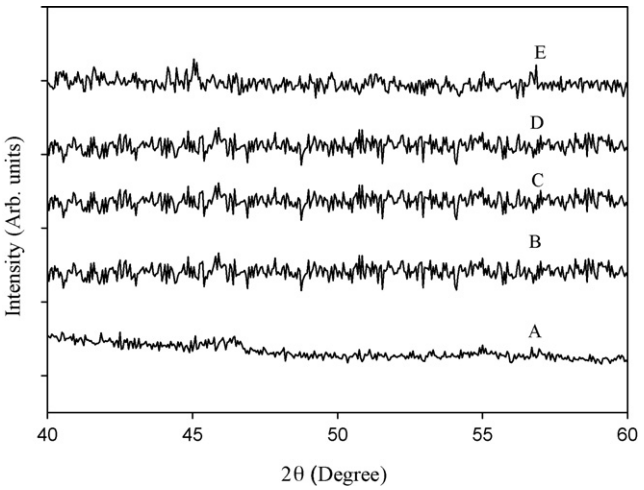

Fig. 1. XRD patterns of Fe–P–B samples. (A) $Fe_{75.6}P_{10.2}B_{14.2}$, (B) $Fe_{85.1}P_{2.1}B_{12.8}$, (C) $Fe_{82.4}P_{1.1}B_{16.5}$, (D) $Fe_{87.3}P_{3.3}B_{9.4}$, and (E) $Fe_{78.6}P_{8.8}B_{12.6}$.

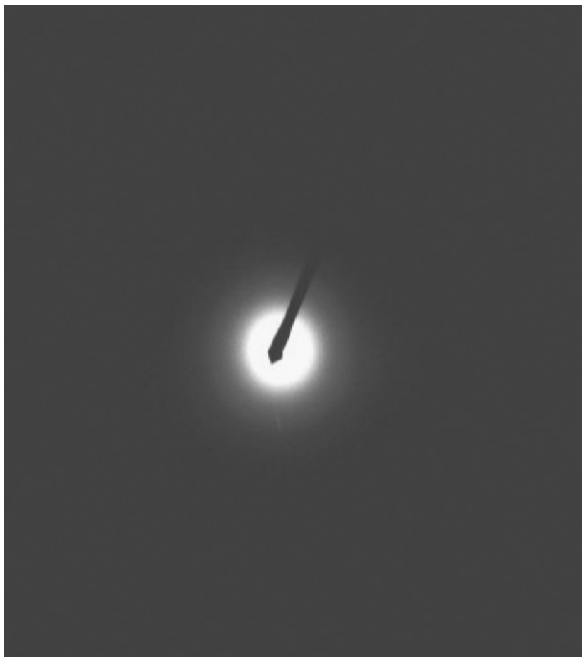

Fig. 2. Electron diffraction image of sample A ($Fe_{75.6}P_{10.2}B_{14.2}$; $FeCl_2$ and H_2O).

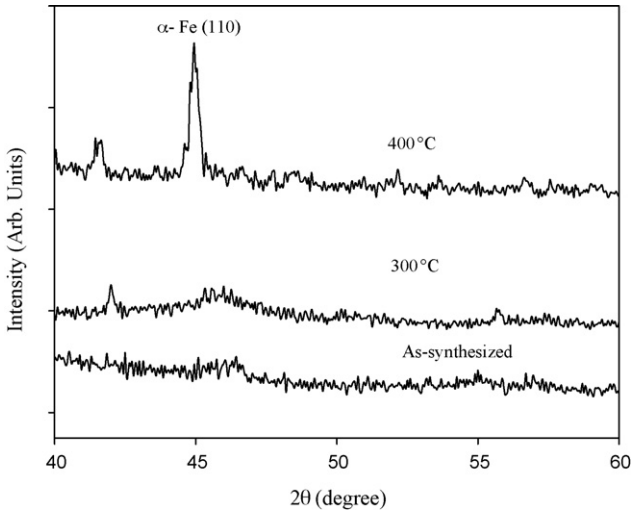

Fig. 3. XRD patterns of sample A ($Fe_{75.6}P_{10.2}B_{14.2}$; $FeCl_2$ and H_2O) upon treatment at 300 and 400 °C.

3. Results and discussion

3.1. Physicochemical properties of Fe–P–B nanoalloys

Fe–P–B samples were characterized by ICP-AES, XRD, TEM, and XPS techniques. Table 1 shows the effect of preparation conditions on the composition of Fe–P–B nanoalloys. The substitution degree of B for P varies with solvent and iron precursor. XRD patterns of as-synthesized Fe–P–B nanoalloys prepared using a molar composition of 1:3:3 are shown in Fig. 1. There is no significant change in the XRD patterns of Fe–P–B alloys due to the effect of solvent and the preparation conditions. All the samples confirm the amorphous nature of Fe–P–B alloys. Fig. 2 shows the electron diffraction image of sample A ($Fe_{75.6}P_{10.2}B_{14.2}$) prepared using $FeCl_2$ as iron precursor in aqueous medium. The broad and diffuse Debye rings further evidences the amorphous nature of the sample. The effect of calcination temperature on the crystalline phase of sample A ($Fe_{75.6}P_{10.2}B_{14.2}$) is demonstrated in Fig. 3. The as-synthesized samples were calcined at 300 and 400 °C for 2 h. The sample retains its

Table 2
Surface area and particle size of Fe–P–B catalysts under various preparation conditions

Catalysts	Surface area (m^2/g)	Particle size (nm)	
		TEM	Estimated average size
A ($Fe_{75.6}P_{10.2}B_{14.2}$)	368	1–10	2.1
B ($Fe_{85.1}P_{2.1}B_{12.8}$)	48	40–50	15.9
C ($Fe_{82.4}P_{1.1}B_{16.5}$)	131	1–10	5.8
D ($Fe_{87.3}P_{3.3}B_{9.4}$)	79	10–20	9.7
E ($Fe_{78.6}P_{8.8}B_{12.6}$)	42	80–100	18.2

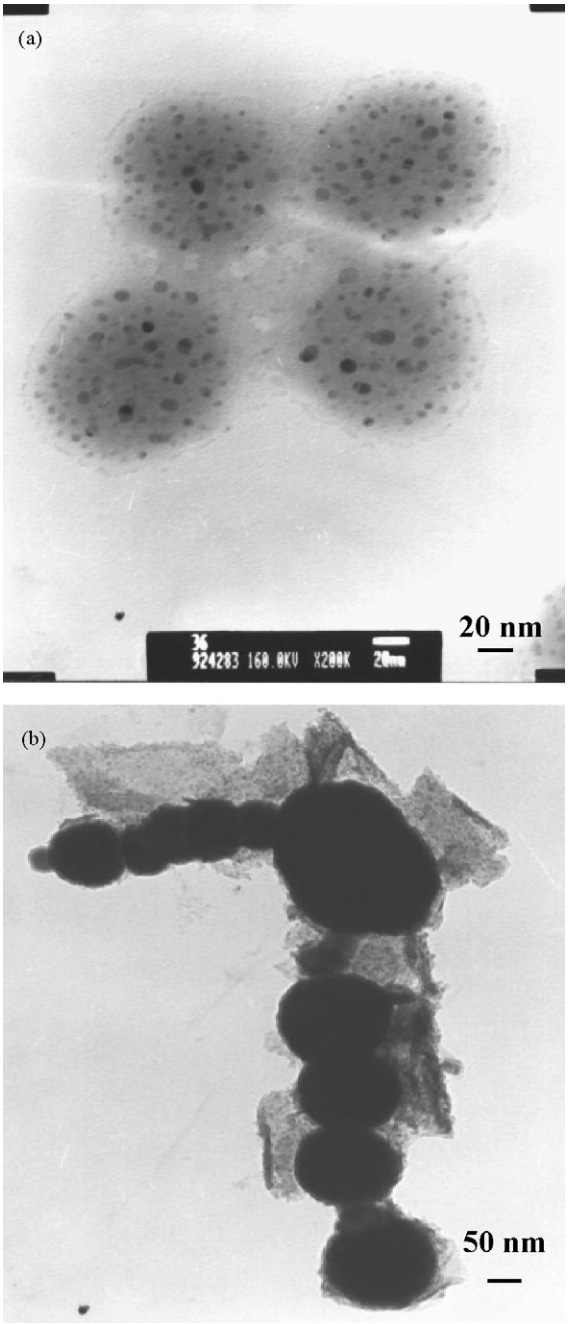

Fig. 4. TEM images of (a) sample A ($Fe_{75.6}P_{10.2}B_{14.2}$; $FeCl_2$ and H_2O) and (b) sample B ($Fe_{85.1}P_{2.1}B_{12.8}$; $FeCl_3$ and H_2O).

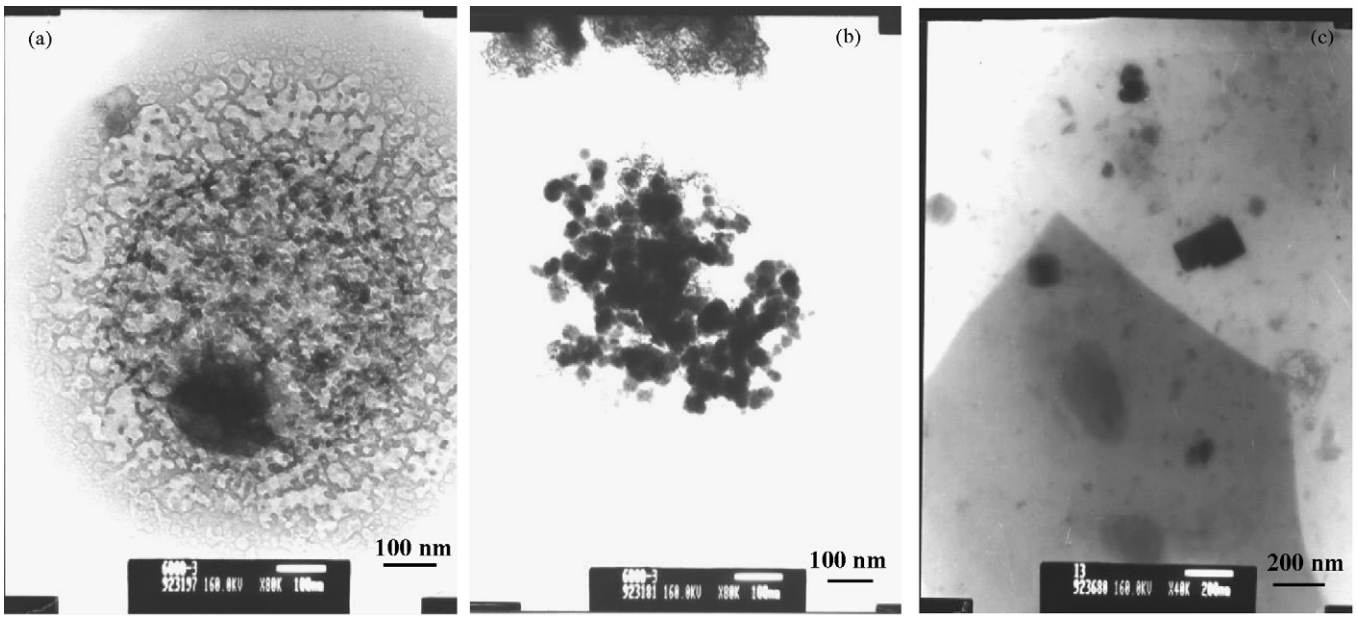

Fig. 5. TEM images of (a) sample C ($Fe_{82.4}P_{1.1}B_{16.5}$; $FeCl_2$ and EtOH/H_2O), (b) sample D ($Fe_{87.3}P_{3.3}B_{9.4}$; $Fe(OA_C)_2$ and EtOH/H_2O), and (c) sample E ($Fe_{78.6}P_{8.8}B_{12.6}$; $Fe(OA_C)_2$ and IPA/H_2O).

amorphous structure until 300 °C and started to crystallize subsequently. The XRD pattern of sample A calcined at 400 °C showed a well-crystallized α-Fe (1 1 0) peak at $2\theta = 44°$. The experimental results revealed that the preparation methods influenced the morphology and particle size of the ultrafine Fe–P–B amorphous alloy catalysts, subsequently affecting the surface areas of the materials. The effect of preparation variables on the surface area of Fe–P–B nanoalloys are shown in Table 2. $Fe_{75.6}P_{10.2}B_{14.2}$ (sample A) prepared in the aqueous solution with the Fe/P/B ratio of 1:3:3 in the mother solution using $FeCl_2$ as iron precursor has the largest surface area of 368 m^2/g and $Fe_{78.6}P_{8.8}B_{12.6}$ (sample E) prepared in 50% IPA solution using $Fe(OAc)_2$ as iron precursor has the lowest surface area of 42 m^2/g. Notably, if the solvent H_2O was replaced with 50% IPA in H_2O, the surface area significantly decreased for Fe–P–B catalysts.

The distinct differences on the morphologies and particle sizes of the samples were observed in TEM micrographs. The sample A ($Fe_{75.6}P_{10.2}B_{14.2}$), sample B ($Fe_{85.1}P_{2.1}B_{12.8}$), sample C ($Fe_{82.4}P_{1.1}B_{16.5}$), and sample D ($Fe_{87.3}P_{3.3}B_{9.4}$) have a spherical or chain-like morphology with apparent boundary, as shown in Figs. 4 and 5. However, sample E ($Fe_{78.6}P_{8.8}B_{12.6}$) has a square morphology, as demonstrated in Fig. 5(c). It can be clearly observed from Table 2 that there is a direct correlation between the particle size and the surface area of Fe–P–B nanoalloys. The particle size distribution obtained from TEM micrographs for samples A, B, C, D, and E are in the range of 1–10, 40–50, 1–10, 10–20, and 80–100 nm, respectively, and the estimated average particle size for samples A, B, C, D, and E are 2.1, 15.9, 5.8, 9.7, and 18.2 nm, respectively. Both samples A and C have a narrow particle size distribution; however, sample A has smaller Fe–P–B particles (2.1 nm) than sample C (5.8 nm). Fe–P–B prepared using $Fe(OAc)_2$ in IPA/H_2O medium has larger Fe–P–B particles, which results in lower surface area. The effect of iron precursor on the surface area and particle size can be observed by comparing samples A and B. When $FeCl_2$ was used as iron precursor instead of $FeCl_3$ in aqueous medium, there was a narrow particle size distribution with nanosized particles.

XPS analysis was used to calculate the surface compositions of Fe–P–B nanoalloys. Table 1 reveals the influence of iron precursor and the preparation medium on the surface composition of the catalysts. The atomic composition on the surface and in the bulk for sample A was $Fe_{81.7}P_{2.0}B_{15.3}$ and $Fe_{75.6}P_{10.2}B_{14.2}$, respectively. XPS spectra of sample A is shown in Fig. 6, while Table 3 shows the binding energy values of Fe–P–B nanoalloys. In Fig. 6 corresponding to the XPS spectra of sample A (curve a), two main peaks of iron with binding energies of 706.9 and 719.6 eV are attributed to the Fe $2p_{3/2}$ and Fe $2p_{1/2}$ levels, respectively. The binding energy of 706.9 eV for Fe $2p_{3/2}$ is consistent with the values for pure iron metal [37]. In addition, a shoulder peak with a binding energy of around 710.3 eV can be assigned to the oxidized iron species on the surface. The relative areas of the main and shoulder peaks of the Fe $2p_{3/2}$ level suggest that Fe in Fe–P–B nanoalloy is mainly present in its metallic state on the surface of the sample. In Fig. 6, curve c is the XPS spectrum of the P_{2p} level on the surface of the sample. The peak with a lower binding energy of 129.8 eV arises from the elemental phosphorus bounded to metallic iron, while the peak with the higher energy of 133.1 eV can be assigned to the oxidized phosphorus species, which are in accordance with the values of the P_{2p} level in NiP system [37]. The binding energy of 129.8 eV for the P_{2p} level is smaller than that of red phosphorus (130.0 eV) and the chemical shift of −0.2 eV results from the electron transfer from

Table 3
XPS binding energy of Fe–P–B catalysts through different treatments

Fe–P–B catalysts[a]	Fe (eV)		B (eV)	P (eV)
	$2p_{3/2}$	$2p_{1/2}$	1s	2p
Before Ar^+ sputtering				
A ($Fe_{75.6}P_{10.2}B_{14.2}$)	710.3	724.9	192.1	133.1
B ($Fe_{85.1}P_{2.1}B_{12.8}$)	711.0	724.6	191.5	133.1
C ($Fe_{82.4}P_{1.1}B_{16.5}$)	711.3	725.4	191.5	131.5
D ($Fe_{87.3}P_{3.3}B_{9.4}$)	711.2	724.8	192.0	132.7
After 10 min Ar^+ sputtering				
A ($Fe_{75.6}P_{10.2}B_{14.2}$)	706.9	719.6	187.0	129.8
B ($Fe_{85.1}P_{2.1}B_{12.8}$)	706.8	719.8	187.1	129.1
C ($Fe_{82.4}P_{1.1}B_{16.5}$)	709.9	724.0	191.8	130.2
D ($Fe_{87.3}P_{3.3}B_{9.4}$)	709.2	723.0	191.2	132.9
E[b] ($Fe_{78.6}P_{8.8}B_{12.6}$)	709.6	723.1	191.2	131.9

[a] Binding energy was corrected by carbon (C_{1s} = 285.0 eV).
[b] Sample after 15 min Ar^+ sputtering.

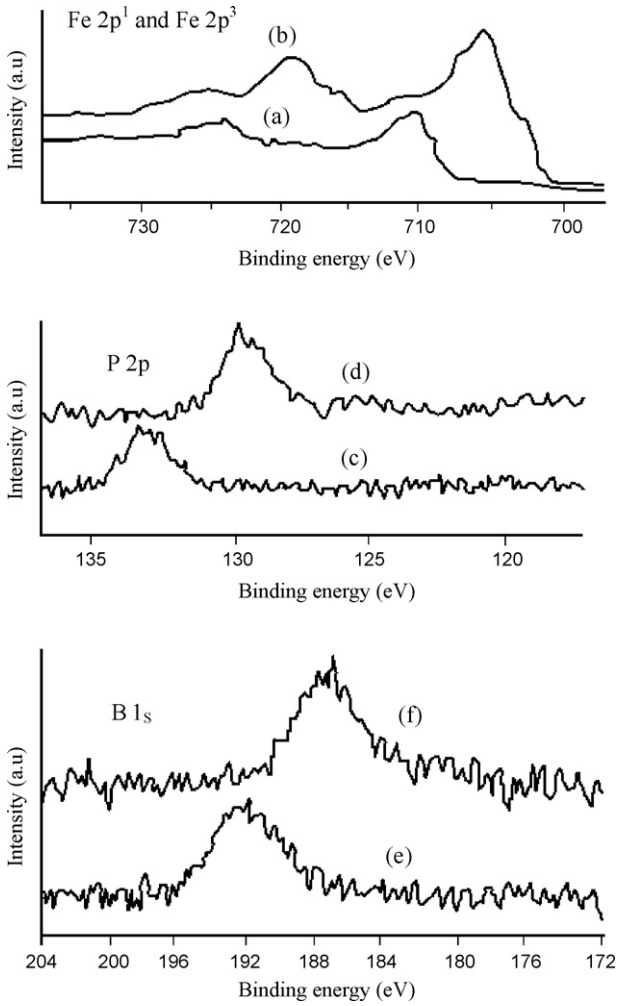

Fig. 6. XPS spectra of sample A ($Fe_{75.6}P_{10.2}B_{14.2}$): a, c, and e—catalyst before Ar^+ sputtering; b, d, and f—catalyst after 10 min Ar^+ sputtering.

iron to phosphorus. As shown in the figure (curve e), the peak for B 1s with the binding energy of 187 eV can be related to the elemental boron bound to metallic iron, while the peak at 192.1 eV can be attributed to the oxidized boron species on the surface of the sample [37]. The chemical shift of –0.3 eV observed for sample A may be due to the electron transfer from boron to iron. There is no significant difference in the XPS spectra of samples A and B. The XPS spectra of sample B also confirms the presence of elemental Fe, P, and B on the surface of the catalyst after Ar^+ sputtering. In contrast, samples C–E did not show any elemental iron and boron even after sputtering for 10 min. The samples prepared with organic solvent have oxidized Fe, P, and B species in the bulk composition as well as on the surface of the particles, whereas the samples prepared with aqueous medium have oxidized species only on the surface.

3.2. Catalytic activity

The dehydrogenation of ethanol was used to test the catalytic behavior of Fe–P–B catalysts. Fig. 7 shows the time-on-stream study on the influence of preparation conditions on the catalytic properties of Fe–P–B catalysts at 250 °C. The reaction selectivity of acetaldehyde on all the catalysts was nearly 100%. Moreover, in this study, the catalytic activity of sample A ($Fe_{75.6}P_{10.2}B_{14.2}$) and the sample D ($Fe_{87.3}P_{3.3}B_{9.4}$) does not show any deactivation. $Fe_{82.4}P_{1.1}B_{16.5}$ catalyst demonstrated the highest initial conversion. The catalytic activities of Fe–P–B catalysts are exhibited in Table 4 and Fig. 8. The catalytic activity per gram of the catalyst was in the following order: sample C ($Fe_{82.4}P_{1.1}B_{16.5}$) > sample D ($Fe_{87.3}P_{3.3}B_{9.4}$) > sample B ($Fe_{85.1}P_{2.1}B_{12.8}$) > sample A ($Fe_{75.6}P_{10.2}B_{14.2}$) > sample E ($Fe_{78.6}P_{8.8}B_{12.6}$). The order of the

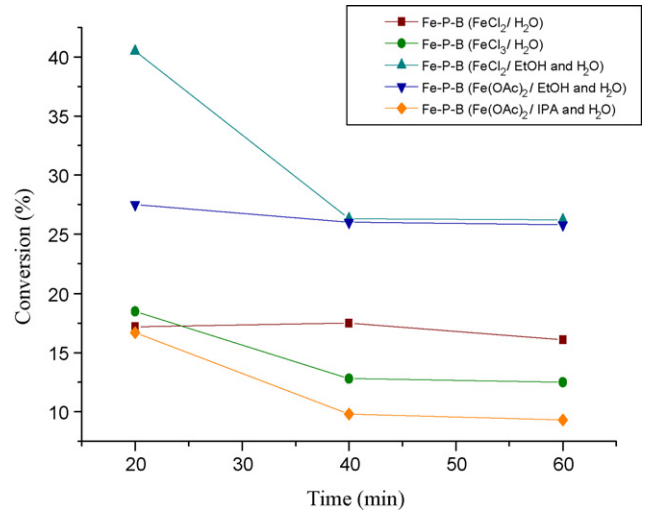

Fig. 7. Reaction conversion of Fe–P–B catalysts vs. time on stream (reaction condition: 250 °C, F/W = 0.01725 mol ethanol/g catalyst/h).

Table 4
Catalytic activity of Fe–P–B catalysts (reaction condition: 250 °C, 1 atm)

Catalysts	Surface area (m^2/g)	Catalytic activity	
		(mole × 10^9)/(g s)	(mole × 10^{10})/(m^2 s)
A ($Fe_{75.6}P_{10.2}B_{14.2}$)	368	41.2	1.1
B ($Fe_{85.1}P_{2.1}B_{12.8}$)	48	44.3	9.2
C ($Fe_{82.4}P_{1.1}B_{16.5}$)	131	97.0	7.4
D ($Fe_{87.3}P_{3.3}B_{9.4}$)	79	51.5	6.5
E ($Fe_{78.6}P_{8.8}B_{12.6}$)	42	40.0	9.5

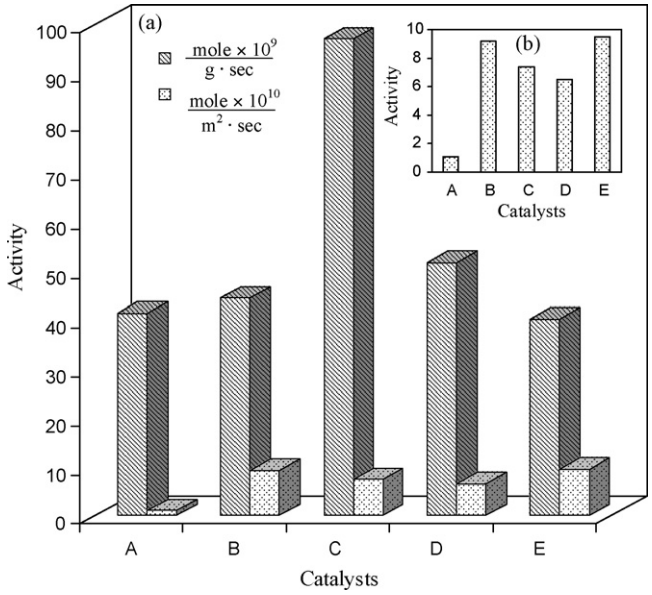

Fig. 8. (a) Dehydrogenation activity of Fe–P–B catalysts (reaction condition: 250 °C, 1 atm) using (A) $Fe_{75.6}P_{10.2}B_{14.2}$, (B) $Fe_{85.1}P_{2.1}B_{12.8}$, (C) $Fe_{82.4}P_{1.1}B_{16.5}$, (D) $Fe_{87.3}P_{3.3}B_{9.4}$, and (E) $Fe_{78.6}P_{8.8}B_{12.6}$; inset (b) shows the specific activity per square meter.

Table 5
Catalytic activity of Fe–P–B catalysts along with its physicochemical properties

Fe/P/B mole in the mother solution	Preparation condition		ICP bulk composition (atomic ratio)	XPS surface composition (atomic ratio)	Surface area (m^2/g)	Particle size (nm)		Catalytic activities	
	Solvent	Iron precursor (0.1 M)				TEM	Estimated average size	(mole × 10^9)/(g s)	(mole × 10^{10})/(m^2 s)
Fe–B (1:0:3)	H_2O/EtOH	$FeCl_2$	$Fe_{53.7}B_{46.1}$	$Fe_{55.4}B_{44.6}$	40	20–30	19.1	43.1	10.8
Fe–P (1:3:0)	H_2O/EtOH	$FeCl_2$	$Fe_{71.7}P_{28.3}$	$Fe_{60.9}P_{39.1}$	106	10–20	7.2	33.8	3.1
Fe–P–B (1:3:3)	H_2O/EtOH	$FeCl_2$	$Fe_{82.4}P_{1.1}B_{16.5}$	$Fe_{84.5}P_{2.5}B_{13.0}$	131	1–10	5.8	97	7.4

specific catalytic activity per surface area of the ethanol dehydrogenation was $Fe_{78.6}P_{8.8}B_{12.6}$ > $Fe_{85.1}P_{2.1}B_{12.8}$ > $Fe_{82.4}P_{1.1}B_{16.5}$ > $Fe_{87.3}P_{3.3}B_{9.4}$ > $Fe_{75.6}P_{10.2}B_{14.2}$. $Fe_{78.6}P_{8.8}B_{12.6}$ catalyst evidenced the highest activity among all the catalysts. According to the results, iron precursor and the medium for the preparation of Fe–P–B significantly affect the concentration of boron and phosphorus bonded to the iron metal, subsequently affecting the activity of the catalysts. Moreover, experimental results indicated that the preparation conditions significantly affect the surface area and the particle size of the Fe–P–B catalysts. The specific activity per gram of $Fe_{82.4}P_{1.1}B_{16.5}$, prepared with $FeCl_2$ in 50% ethanol solution, showed the highest activity among all the Fe–P–B catalysts. The enhanced catalytic activity can be related to its narrow particle size distribution and the concentration of Fe, P, and B. In the case of sample C, the substitution of B for P is higher than other catalysts, which may be the reason for the highest activity. However, $Fe_{78.6}P_{8.8}B_{12.6}$, prepared with $Fe(OAc)_2$ in 50% IPA solution showed the highest specific activity per surface area among all the Fe–P–B catalysts.

3.3. Effect of B substitution on the catalytic activity of Fe–P–B nanoalloys

Table 5 shows the correlation of physicochemical properties with catalytic activity and the effect of B substitution on Fe–P–B nanoalloys. It can be observed that the surface area of Fe–P increased from 106 to 131 m^2/g following substitution of B for P. Similarly, there is a great influence of B substitution on the particle size of Fe–P–B. The presence of B changes the morphology of Fe–P–B and narrows the particle size distribution from 10–20 to 1–10 nm. The specific activity per weight of the catalyst was compared and Fe–P–B has higher activity than Fe–P and Fe–B, which may be due to the presence of B and high surface area of the catalyst. The high activity of this catalyst can be attributed to both high surface area and high turnover frequency (TOF). However, Fe–P has the highest specific activity per surface area.

4. Conclusion

By the comparison of Fe–P–B nanoalloys prepared using chemical reduction method, it could be concluded that the catalytic activity of the catalysts for the dehydrogenation of ethanol is related to the particle size, surface area, and the surface composition of Fe–P–B. Iron precursors and the reaction medium play a major role in determining the structure, morphology, and composition of Fe–P–B. The replacement of H_2O with 50% ethanolic solution or 50% isopropyl alcoholic solution, the surface area decreased drastically. Fe–P–B materials prepared with $FeCl_2$ has higher surface area than those prepared by $FeCl_3$ and $Fe(OAc)_2$. XRD patterns of the as-synthesized Fe–P–B materials confirm the amorphous state. The preparation methods significantly affected the concentration of boron and phosphorus bonded to the iron metal, subsequently affecting the composition of these materials. The specific activity per gram of $Fe_{82.4}P_{1.1}B_{16.5}$, prepared with $FeCl_2$ and EtOH, showed the highest value among all the Fe–P–B catalyst. The specific activity per surface area of $Fe_{78.6}P_{8.8}B_{12.6}$, prepared with $Fe(OAc)_2$ and IPA showed the highest activity among all the Fe–P–B catalysts.

Acknowledgment

This research was supported by the Ministry of Economic Affairs, Taiwan, Republic of China, under contract number 94-EC-17-A09-S1-022.

References

[1] K. Klement Jr., R.H. Willens, P. Duwez, Nature (London) 187 (1960) 869.
[2] M. Shibata, T. Masumoto, Prep. Catal. 4 (1987) 353.
[3] A. Molnar, G.V. Smith, M. Bartok, Adv. Catal. 36 (1989) 329.
[4] H. Yamashita, M. Yoshikawa, T. Funabiki, S. Yoshida, J. Chem. Soc., Faraday Trans. I 81 (1981) 2485.
[5] H. Yamashita, T. Faminade, T. Funabiki, S. Yoshida, J. Mater. Sci. Lett. 4 (1985) 1241.
[6] H. Yamashita, T. Funabiki, S. Yoshida, J. Chem. Soc., Chem. Commun. (1984) 868.
[7] H. Yamashita, M. Yoshikawa, T. Funabiki, S. Yoshida, J. Catal. 99 (1986) 375.
[8] H. Yamashita, M. Yoshikawa, T. Funabiki, S. Yoshida, J. Chem. Soc., Faraday Trans. I 82 (1986) 1771.
[9] S. Yoshida, H. Yamashita, T. Funabiki, T. Yonezawa, J. Chem. Soc., Chem. Commun. (1982) 964.
[10] S. Yoshida, H. Yamashita, T. Funabiki, T. Yonezawa, J. Chem. Soc., Faraday Trans. I 80 (1984) 1435.
[11] S. Yoshida, H. Yamashita, T. Funabiki, Hyomen 24 (1986) 349.
[12] A. Yokoyama, H. Komiyama, H. Inoue, T. Masumoto, H.M. Kimura, J. Catal. 68 (1981) 355.
[13] A. Yokoyama, H. Komiyama, H. Inoue, T. Masumoto, H.M. Kimura, J. Chem. Soc. Jpn. 2 (1982) 199.
[14] M. Shibata, Y. Ohbayashi, N. Kawata, T. Masumoto, K. Aoki, J. Catal. 96 (1985) 296.
[15] H.I. Schlesinger, H.C. Brown, A.E. Finholt, J.R. Gilbreath, H.R. Hoekstra, E.K. Hyde, J. Am. Chem. Soc. 74 (1953) 215.
[16] S. Linderoth, S. Mørup, J. Appl. Phys. 69 (8) (1991) 5256.
[17] J. Saida, A. Inoue, T. Masumoto, Metall. Trans. A 22 (1991) 2125.
[18] J.Y. Shen, Z.Y. Li, Q.J. Yan, Y. Chen, J. Phys. Chem. 97 (1993) 8564.
[19] S. Linderoth, S. Mørup, J. Appl. Phys. 67 (1990) 4472.
[20] J. Shen, Z. Li, Q. Zhang, Y. Chen, Q. Bao, Z. Li, in: L. Guczi, F. Solymosi, P. Tetenyi (Eds.), New Frontiers in Catalysis, Akademiai1 Kiado, Budapest, 1993, p. 2193.
[21] J. Deng, X. Zhang, Appl. Catal. 37 (1988) 339.
[22] Z. Hu, J.Y. Shen, Y. Chen, M. Lu, Y.F. Hsia, J. Non-Crystal. Solids 159 (1993) 88.
[23] Z. Hu, J. Shen, Y. Fan, Y. Hsia, Y. Chen, J. Mater. Sci. Lett. 12 (1993) 1020.
[24] J. Shen, Q. Zhang, Z. Li, Y. Chen, J. Mater. Sci. Lett. 15 (1996) 715.
[25] J. Deng, X. Zhang, Solid State Ionics 32–33 (1989) 1006.
[26] J.Y. Shen, Z. Hu, Y.F. Hsia, Y. Chen, J. Phys. 4 (1992) 6381.
[27] Z. Hu, Y. Chen, Y.F. Hsia, Nucl. Instrum. Meth. Phys. Res. B 76 (1993) 121.
[28] Z. Hu, Y. Fan, Y. Wu, Q. Yan, Y. Chen, J. Magn. Magn. Mater. 104–144 (1995) 413.
[29] J. Shen, Z. Hu, Q. Zhang, L. Zhang, Y. Chen, J. Appl. Phys. 71 (1992) 5217.
[30] B. Rajesh, N. Sasirekha, Y.-W. Chen, J. Mol. Catal. A 275 (2007) 174.
[31] Z. Hu, Y. Fan, F. Chen, Y. Chen, J. Chem. Soc. Chem. Commun. 247 (1995).
[32] B. Rajesh, N. Sasirekha, Y.-W. Chen, S.-P. Lee, Ind. Eng. Chem. Res. 46 (2007) 2034.
[33] M.L. Fdez-Gubieda, A. García-Arribas, J.M. Barandiarán, J. Herreros, Physica B 208–209 (1995) 363.
[34] S.C. Perera, P.S. Fodor, G.M. Tsoi, L.E. Wenger, S.L. Brock, Chem. Mater. 15 (2003) 4034.
[35] V.V. Hoang, Physica B 348 (2004) 347.
[36] C.Y. Lin, T.S. Chin, S.X. Zhou, Z.C. Lu, L. Wang, F.F. Chen, M.X. Pan, W.H. Wang, J. Magn. Magn. Mater. 282 (2004) 156.
[37] Y. Okamoto, Y. Nitta, T. Imanaka, S. Teranishi, J. Chem. Soc., Faraday Trans. 1 75 (1979) 2027.